RSC Advances

PAPER

View Article Online
View Journal | View Issue

Cite this: *RSC Adv.*, 2022, **12**, 21609

Glutathione-depleting polymer delivering chlorin e6 for enhancing photodynamic therapy†

Shi-yin Wang,‡[a] Guo Chen,‡[a] Ji-feng Chen,[a] Jin Wang,[b] Shao-hui Deng*[a] and Du Cheng *[a]

The therapeutic effect of photodynamic therapy (PDT) is highly dependent on the intracellular production of reactive oxygen species (ROS). However, the ROS generated by photosensitizers can be consumed by the highly concentrated glutathione (GSH) in tumor cells, severely impairing the therapeutic effect of PDT. Herein, we synthesized a GSH-scavenging copolymer to deliver photosensitizer chlorin e6 (Ce6). The pyridyl disulfide groups, which have faster reactivity with the thiol groups of GSH than other disulfide groups, were grafted onto a hydrophobic block to encapsulate the Ce6. Under NIR irradiation, the Ce6 generated ROS to kill tumor cells, and the pyridyl disulfide groups depleted the GSH to prevent ROS consumption, which synergistically enhanced the therapeutic effect of PDT. *In vitro* and *in vivo* experiments confirmed the combinatory antitumor effect of Ce6-induced ROS generation and the pyridyl disulfide group-induced GSH depletion. Therefore, the pyridyl disulfide group-grafted amphiphilic copolymer provides a more efficient strategy for enhancing PDT and has promising potential for clinical application.

Received 23rd March 2022
Accepted 16th July 2022

DOI: 10.1039/d2ra01877b

rsc.li/rsc-advances

Introduction

Photodynamic therapy (PDT) has drawn tremendous attention in cancer therapy due to its spatiotemporally controlled feature which minimizes damage to normal tissues.[1,2] In general, PDT utilizes photosensitizers (PS) to convert oxygen into toxic reactive oxygen species (ROS) for killing cancer cells when irradiated with a near-infrared (NIR) laser,[3,4] which means that its therapeutic effect is highly dependent on the intracellular production of ROS.[5,6]

The photosensitizer concentration in tumor tissue is a key factor for enhancing the generation of ROS.[7,8] However, the majority of PSs are hydrophobic, including chlorin e6 (Ce6),[9–11] porphyrin derivatives,[12,13] and boron-dipyrromethene (BODIPY) derivatives.[14,15] Although these PSs exhibit efficient ROS generation upon irradiation, free PSs are difficult to accumulate in a tumor and enter into cells.[16,17] Nowadays, some nanocarriers including micelles and liposomes have been developed and approved for use in the clinic.[18–20] Nanocarriers can not only load hydrophobic PSs with high efficiency, but also effectively deliver them into tumor cells. Thus, utilizing nanocarriers delivering PSs is an effective approach for increasing ROS generation.

Another challenge for PDT is that the PS-induced ROS can be consumed by glutathione (GSH), a key intracellular antioxidant, severely impairing the therapeutic effect of PDT.[21,22] Worse still, GSH in tumor cells is overexpressed with several-fold higher concentration (up to 10 mM) than that in normal cells.[23,24] Thus, consuming intracellular GSH is believed to be a direct and efficient strategy for enhancing the therapeutic efficacy of PDT.[6,25,26] Considering the intrinsic property of the GSH thiol group, the most straightforward way to consume intracellular GSH is the introduction of some chemical groups that can react with the thiol group of GSH.[26–29]

Inorganic nanoparticles, such as oxidizing metal ions, mostly deplete GSH in a nonspecific way, and exhibit poor biocompatibility and unavoidable metabolic toxicity.[30,31] Organic nanoparticles, such as alkenes and maleimides,[32] induce GSH depletion only under alkaline pH conditions, making them difficult to use widely.[33] Notably, disulfide–thiol exchange is a typical reaction to oxidize the thiol group for GSH depletion.[34] Recently, disulfide bonds were introduced into nanocarriers to enhance PDT efficacy through disulfide–thiol exchange-induced GSH consumption.[35–38] However, the incomplete reaction between the disulfide bond and the thiol group limited the efficiency of GSH depletion.[39] Thus, an alternative GSH-depleting agent is desirable to achieve a complete disulfide–thiol exchange reaction to enhance the PDT outcome. It is well known that the pyridyl disulfide group has been extensively used for bioconjugation due to its significantly faster reactivity

[a]*PCFM Lab of Ministry of Education, School of Materials Science and Engineering, Sun Yat-sen University, Guangzhou 510275, P. R. China. E-mail: dengshh9@mail.sysu.edu.cn; chengdu@mail.sysu.edu.cn*

[b]*Department of Radiology, The Third Affiliated Hospital of Sun Yat-sen University, Guangzhou 510630, P. R. China*

† Electronic supplementary information (ESI) available. See https://doi.org/10.1039/d2ra01877b

‡ The authors contributed equally to this work.

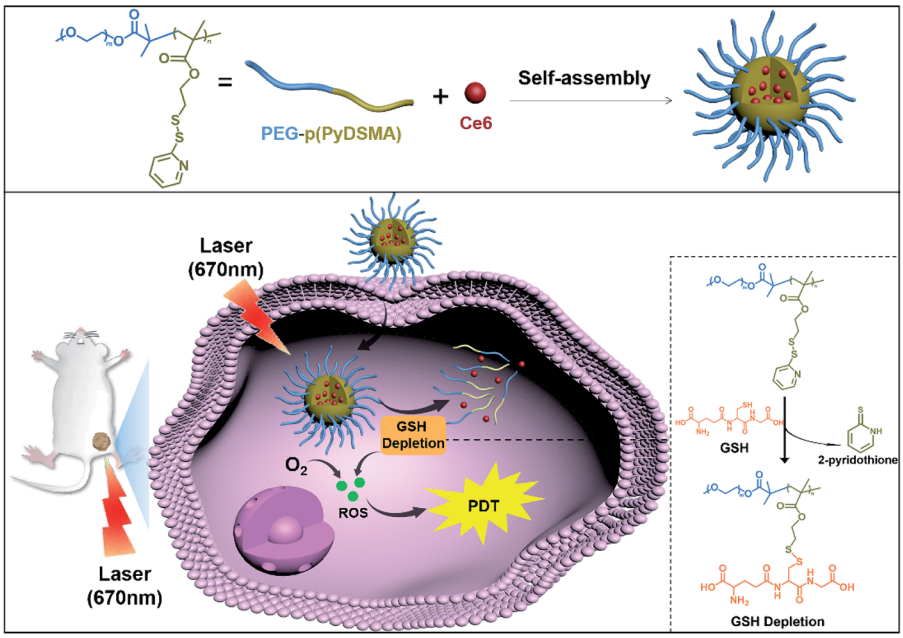

Scheme 1 Schematic illustration of GSH-depleting nanoparticle SS-Py@Ce6 for enhanced photodynamic therapy. Photosensitizer Ce6 and GSH-depleting polymer PEG–p(PyDSMA) were self-assembled into micelles SS-Py@Ce6. The micelles SS-Py@Ce6 were intravenously injected and the tumor tissue was exposed to 670 nm light irradiation. After cellular internalization, SS-Py@Ce6 effectively consumed the intracellular high concentration of GSH attributed to the disulfide–thiol exchange between the pendant pyridyl disulfide groups in PEG–p(PyDSMA) and the thiol groups in GSH. Subsequently, GSH depletion broke the redox homeostasis in tumor cells and improved intracellular ROS generation and accumulation, exhibiting significant enhancement in PDT.

with thiols compared to most other disulfide groups.[40,41] It was reported that pyridyl disulfide had a high exchange efficiency of almost 100% and resulted in a stable product: tautomeric 2-pyridothione.[39,42] At present, there have been few reports about using pyridine disulfide groups to deplete GSH.[43,44] Therefore, to introduce pyridyl disulfide groups into a nanocarrier might be a more effective strategy for consuming intracellular GSH.

Considering that a nanocarrier with an uncomplicated structure might have more potential in clinical applications,[45,46] we synthesized an amphiphilic diblock copolymer of monomethoxy-poly(ethylene glycol)-*b*-poly(pyridyl disulfide ethyl methacrylate), abbreviated as PEG–p(PyDSMA), to achieve both GSH depletion and hydrophobic PS delivery. The hydrophobic block p(PyDSMA) not only served as the hydrophobic core of a micelle to load Ce6, but also consumed GSH through the pendant pyridyl disulfide groups. In the tumor cells, the pyridyl disulfide groups in the p(PyDSMA) efficiently reacted with the thiol groups in the GSH to consume intracellular GSH, which increased the sensitivity of tumor cells to NIR/Ce6-induced oxidative stress. Therefore, we believe that the GSH-depleting nanocarrier shows excellent clinical potential for PDT against cancer (Scheme 1).

Experimental

Materials

Methoxy polyethylene glycols (mPEG, 2 kDa), 2,2′-dipyridyl disulfide (DPDS), 2-(2-hydroxyethyl) pyridine, methacryloyl chloride, and chlorin e6 (Ce6) were purchased from J&K Scientific Ltd (Beijing, China). Carbon disulfide (CS_2), 1-dodecanethiol ($C_{12}H_{26}S$), 18-crown 6-ether ($C_{12}H_{24}O_6$) and triethylamine (TEA) were purchased from Aladdin Co. (China). 2-Mercaptoethanol (C_2H_6OS) and 2,2′-azobisisobutyronitrile (AIBN) were purchased from 3A Chemicals Co. (China). Glacial acetic acid (AcOH), acetone, methanol (MeOH), dichloromethane (DCM), dimethyl ether (Et_2O), isopropyl alcohol (IPA), 1,4-dioxane ($C_4H_8O_2$), *N*,*N*-dimethylformamide (DMF) and other frequently-used chemical reagents were purchased from Guangzhou Chemical Reagent Company (Guangzhou, China). Human nasopharyngeal carcinoma cells (CNE-2) were provided from the Cell Bank of the Chinese Academy of Sciences (Shanghai, China). Cell culture medium RPMI-1640, phosphate-buffered saline (PBS), fetal bovine serum (FBS), and 0.25% trypsin were obtained from Gibco BRL (Carlsbad, CA, USA). Hoechst 33342, 1,1′-dioctadecyl-3,3,3′,3′-tetramethyl indotricarbocyanine iodide (DiR), dichlorofluorescein (DCF), annexin V-FITC, propidium iodide (PI) and other fluorescent staining agents were supplied by Yeasen Biotechnology Co. Ltd (Shanghai, China).

Preparation of GSH-depleting SS-Py@Ce6 nanoparticles and GSH-nondepleting Py@Ce6 nanoparticles

GSH-depleting polymer PEG–p(PyDSMA) and GSH-nondepleting polymer PEG–p(PyEMA) were synthesized by reversible addition–fragmentation chain transfer polymerization (RAFT). The synthesis details are described in the ESI.† To

prepare GSH-depleting SS-Py@Ce6 nanoparticles and GSH-nondepleting Py@Ce6 nanoparticles, the polymers (10 mg) PEG–p(PyDSMA) and PEG–p(PyEMA) were respectively dissolved in 1 mL of dimethyl sulfoxide (DMSO), and further mixed with 100 μL of Ce6 solution (10 mg mL^{-1}, solvent: DMSO). The mixture was dispersed into 10 mL of deionized water and self-assembled to form Ce6-encapsulated micelles under ultrasound (60 Sonic Dismembrator, Fisher Scientific, USA). A Millipore Centrifugal Filter Device (MW cut-off: 100 kDa) and a syringe filter (pore size: 0.22 μm) were successively used for purification. Finally, the Ce6-encapsulated GSH-depleting SS-Py@Ce6 micelles and GSH-nondepleting Py@Ce6 micelles were obtained (with 1 mg mL^{-1} as the final concentration).

Characterization of SS-Py@Ce6 nanoparticles

^{1}H-NMR spectra were analyzed to verify the successful synthesis of monomers and polymers with a 400 MHz spectrometer (Bruker, Germany) in $CDCl_3$. Gel permeation chromatography (Water Breeze, USA) was used to determine molecular weights and the polymer dispersity index (PDI). Sizes and zeta potentials of the Ce6-encapsulated GSH-depleting SS-Py@Ce6 micelles and GSH-nondepleting Py@Ce6 micelles were obtained with a Zetasizer Nano ZS analyzer (Malvern Instruments Ltd, UK). Transmission electron microscope (TEM) images of SS-Py@Ce6 and Py@Ce6 were recorded with a JEM-1400 Plus (JEOL, Japan) system at 120 kV. Samples (10 μL, 200 μg mL^{-1}) were fixed onto a carbon-coated copper grid and stained by phosphotungstic acid solution before TEM analysis.

Detection of extracellular ROS generation

Fluorescence spectra were used to detect extracellular ROS generation by GSH-depleting SS-Py@Ce6 and GSH-nondepleting Py@Ce6. In brief, a fluorescence probe DCFH-DA (1 eq., 1 mmol L^{-1}) was dissolved in DMSO and hydrolyzed with NaOH solution (40 eq., 10 mmol L^{-1}) at room temperature in the dark. After 30 min of reaction, PBS solution (10 mL) was added. The DCFH solution was well kept in a refrigerator at 4 °C in the dark. Then samples of different groups (*i.e.*, SS-Py@Ce6 (+L), SS-Py@Ce6+10 mM GSH (−L), SS-Py@Ce6+10 mM GSH (+L), Py@Ce6 (+L), Py@Ce6+10 mM GSH (−L), and Py@Ce6+10 mM GSH (+L)) were mixed with 5×10^{-6} mmol L^{-1} DCFH solution (the laser groups were exposed to NIR irradiation (670 nm, 100 mW cm^{-2}, 10 min)). ROS produced by photosensitizer Ce6 subsequently oxidized DCFH to fluorescent DCF. And the ROS generation level was determined by DCF fluorescence (excitation wavelength = 485 nm) using a spectrofluorophotometer (PerkinElmer Ltd, UK). To quantitively explore the influence of GSH on ROS generation in the different nanoparticle groups under irradiation, the nanoparticles (*i.e.*, SS-Py@Ce6, SS-Py@Ce6+10 mM GSH, Py@Ce6, Py@Ce6+10 mM GSH) were mixed with DCFH solution. Then the fluorescence intensities of different groups were recorded at different time points of irradiation (0 min, 2 min, 4 min, 6 min, 8 min, 10 min) with the spectrofluorophotometer (PerkinElmer Ltd, UK).

GSH-depletion assay of SS-Py@Ce6

To verify the GSH-depletion ability of SS-Py@Ce6, UV-vis spectra were used to detect the characteristic absorption peaks of GSH-depleting polymer. The pyridyl disulfide groups on the side chains of PEG–p(PyDSMA) polymer would exchange with the thiol groups of intracellular GSH. This reaction consumed GSH and produced stable tautomeric 2-pyridothione whose characteristic absorption peak for UV-vis spectra is at 343 nm. The GSH-depletion ability of the nanoparticles was characterized by the characteristic absorption peak of 2-pyridothione in the UV-vis spectra. SS-Py@Ce6 and Py@Ce6 nanoparticles with/without 10 mM GSH were detected with an Agilent Cary 60 UV-vis spectrophotometer with detection wavelengths from 300 nm to 700 nm.

Stability of SS-Py@Ce6 and by-product to ROS

The stability of SS-Py@Ce6 and by-product 2-pyridothione to ROS was also determined by UV-vis spectra. The spectra of SS-Py@Ce6 and SS-Py@Ce6 nanoparticle solutions mixed with 60 μM 2-pyridothione were recorded with the Agilent Cary 60 UV-vis spectrophotometer. Then the above solutions were exposed to light irradiation (670 nm, 100 mW cm^{-2}, 30 min). The UV-vis spectra after illumination were recorded to verify the stability of SS-Py@Ce6 and 2-pyridothione.

Cell culture and animal model

The human NPC CNE-2 cell line was purchased from the Cell Bank of the Chinese Science Academy (Shanghai, China). RPMI-1640 medium supplemented with 10% fetal bovine serum and 1% penicillin-streptomycin was used to culture the CNE-2 cells. The cells were cultured at 37 °C under a humidified atmosphere with 5% CO_2. Nude mice (6 weeks old) were purchased from Guangdong Medical Laboratory Animal Center. To establish a subcutaneously implanted tumor model, 3×10^7 CNE-2 cells were subcutaneously injected into the arm pit of the mice. When tumor volumes reached about 100 mm^3, the mice were ready to receive treatment.

Cellular uptake and distribution *in vitro* of SS-Py@Ce6

The cellular uptake efficiency and distribution of GSH-depleting SS-Py@Ce6 and GSH-nondepleting Py@Ce6 were determined by confocal laser scanning microscopy (CLSM) and flow cytometry analysis. The human nasopharyngeal carcinoma cells (CNE-2) were cultured and incubated with RPMI-1640 medium (10% FBS) overnight at 37 °C (5% CO_2). Then, the CNE-2 cells were incubated with medium containing GSH-depleting SS-Py@Ce6 or GSH non-depleting Py@Ce6 for 4 h. After that, the medium was replaced and the CNE-2 cells were incubated with fresh medium without nanoparticles for another 2 h. Before observation, Hoechst 33342 (10 μg mL^{-1}) was used to stain the cell nuclei. The cellular uptake behavior and distribution of the nanoparticles were observed and recorded by confocal laser scanning microscopy (CLSM, Leica SP8, Germany). The cellular uptake efficiency of GSH-depleting SS-Py@Ce6 or GSH-nondepleting Py@Ce6 was quantified by flow cytometry

analysis (Attune NxT, Invitrogen, America). And the untreated cells were set as a control. For flow cytometry analysis, the CNE-2 cells were incubated using the same procedure as above. After transfection, the cells were collected, trypsinized and resuspended in 1 × PBS for detection by flow cytometry analysis.

Cell viability and apoptosis

The cytotoxicities of GSH-depleting SS-Py@Ce6 and by-product 2-pyridothione to CNE-2 cells were determined by MTT assay. For cytotoxicity analysis of GSH-depleting SS-Py@Ce6, the CNE-2 cells were seeded into 96-well plates (5×10^3 cells per well) and treated with Py@Ce6 and SS-Py@Ce6 nanoparticles at different Ce6 concentrations (0.2, 0.4, 0.6, 0.8 and 1.0 μg mL^{-1}) and the corresponding Ce6-encapsulated polymer concentrations (2.1, 4.2, 6.3, 8.4 and 10.5 μg mL^{-1}), respectively. Then, the groups of SS-Py@Ce6+L and Py@Ce6+L were exposed to NIR irradiation (670 nm, 100 mW cm^{-2}, 2 min). After irradiation, the CNE-2 cells were incubated with fresh RPMI-1640 medium containing 10% FBS. Then MTT solution was added into the medium and the cells were further incubated for 4 h. A microplate reader (BioTek) was used to record the absorbance at 570 nm of each sample. The cell viability was analyzed and quantitively calculated. For cytotoxicity analysis of by-product 2-pyridothione, the CNE-2 cells were treated with different concentrations of 2-pyridothione. The procedure was the same as above.

Cell apoptosis was studied by flow cytometry. The CNE-2 cells were seeded into 12-well plates (2×10^5 cells per well) and treated with PBS, Py@Ce6 or SS-Py@Ce6 nanoparticles at Ce6 concentrations of 1 μg mL^{-1}. The cells of the laser groups were replaced with fresh medium and exposed to NIR irradiation (670 nm, 100 mW cm^{-2}, 2 min). The CNE-2 cells were further cultured for 12 h at 37 °C. Then, the cells were trypsinized, collected, and stained with 5 μL of annexin V-FITC/PI dye for 15 min in the dark. Cell apoptosis was detected by a CytoFLEX flow cytometer (Beckman Coulter, Inc. Brea, CA, USA) and analyzed by FlowJo V10 software.

Analysis of intracellular ROS levels

Intracellular ROS levels were determined by confocal laser scanning microscopy (CLSM) and flow cytometry analysis. 2′,7′-Dichlorofluorescin diacetate (DCFH-DA, Abcam) was employed as a probe for intracellular reactive oxygen species (ROS). The CNE-2 cells were seeded into a 20 mm confocal plate and incubated with different treatments (PBS, Py@Ce6, SS-Py@Ce6, Py@Ce6+L or SS-Py@Ce6+L nanoparticles at Ce6 concentrations of 1 μg mL^{-1}). After 4 h of transfection, the medium was replaced and the probe DCFH-DA was added into the medium. After irradiation and another 30 min of incubation, cell nuclei were stained with Hoechst 33342 (10 μg mL^{-1}). Intracellular ROS generation was observed by CLSM (Ex = 488 nm, Em = 525 nm) and quantitatively analyzed by flow cytometry. The CNE-2 cells were plated into 12-well plates (2×10^5 cells per well). The procedures of transfection and irradiation were the same as above. Then the CNE-2 cells were trypsinized and collected for flow cytometry analysis.

Detection of intracellular GSH depletion

Intracellular GSH depletion was characterized with a commercial reduced GSH assay kit. The CNE-2 cells were seeded at a density of 1×10^7 cells per well and treated with PBS+GSH, Py@Ce6+GSH, SS-Py@Ce6+GSH, Py@Ce6+GSH+L or SS-Py@Ce6+GSH+L. After treatment, the medium was replaced with fresh PBS. The disrupted cell solutions were mixed with GSH detection reagent for 10 min. The absorbance at 412 nm was measured and recorded. The relative intracellular GSH levels of different groups were calculated as follows:

$$\text{relative GSH level } (\%) = \frac{(A_1 - A_2)}{(A_1 - A_0)} \times 100\%$$

A_0, A_1, and A_2 are the absorbances at 412 nm of the blank samples, control group, and experimental group, respectively.

Western blot analysis

GSH depletion induced by the exchange reaction with the pyridyl disulfide groups of the polymer results in the down-regulation of GPX4 protein. To further verify the intracellular GSH-depletion ability of the SS-Py@Ce6 nanoparticles at protein expression level, western blot analysis was conducted. The CNE-2 cells received different treatments (PBS, Py@Ce6, SS-Py@Ce6, Py@Ce6+L, or SS-Py@Ce6+L nanoparticles at Ce6 concentrations of 1 μg mL^{-1}). Then RIPA lysis buffer lysed the CNE-2 cells to extract proteins. After separation by SDS-PAGE electrophoresis, the proteins were transferred onto a PVDF membrane (Millipore Corp. USA). Then 8000× dilutions of primary antibodies specific for GPX4 (Proteintech) and β-actin (Sigma) were added. A chemiluminescence imaging system (GE ImageQuant LAS 500, USA) was used to visualize the protein bands.

In vivo biodistribution of SS-Py@Ce6

The *in vivo* biodistribution of SS-Py@Ce6 was imaged using a Carestream IS 4000 imaging system. NIR fluorescent dye DiR was encapsulated by the GSH-depleting polymer PEG–p(PyDSMA) to form fluorescent SS-Py@DiR nanoparticles. Nude mice bearing tumors were intravenously injected with SS-Py@DiR nanoparticles (at the dose of 400 μg kg^{-1}). Then the kinetic *in vivo* fluorescence distribution was recorded at certain different time points (0, 3, 6, 9, 12, 24, and 48 h post injection). At 48 h after injection, the mice were dissected. The fluorescence of the excised organs (heart, liver, spleen, lung, and kidneys) and tumors were recorded using a Carestream live-animal imaging system.

In vivo antitumor efficiency

The CNE-2 tumor xenograft-bearing nude mice were randomly divided into five groups ($n = 5$) after the tumor volumes reached 100 mm^3. The mice were intravenously injected with 100 μL of PBS, Py@Ce6 or SS-Py@Ce6 nanoparticles. At 6 h after injection, the Py@Ce6+L and SS-Py@Ce6+L groups were exposed to NIR irradiation at the tumor sites of the mice (670 nm, 100 mW cm^{-2}, 10 min). The injection was performed on days 0, 3, 6, and

9. The perpendicular diameters of the tumors were measured with callipers and the tumor volumes of each mouse were recorded every three days after the treatment. (tumor volumes = (length × width^2)/2). At 18 days after the first drug administration, the mice were sacrificed and dissected to obtain the excised solid tumors. The excised tumors were collected and photographed. The weights of the excised tumors were recorded. H&E staining and apoptotic TUNEL assays were performed on the excised tumor tissue sections to reveal the anti-tumor efficacy of different treatments. To determine the survival rate, the CNE-2 tumor xenograft-bearing nude mice were randomly divided into five groups (n = 6) and intravenously injected with various formulations as above. The mice were euthanized when the tumor volume reached 2000 mm^3. The survival rate of the mice was recorded.

Ethics statement

Nude mice (6 weeks old) were purchased from Guangdong Medical Laboratory Animal Center. All the mice received human care in compliance with the regulations of the Animal Care and Use Committee of Sun Yat-sen University (Guangzhou, China). All animal experiments were performed according to the guidelines for Care and Use of Laboratory Animals of the National Institutes of Health (NIH publication no. 85-23, revised 1996) and approved by the Animal Ethics Committee of Sun Yat-sen University (Guangzhou, China).

Statistical analysis

Data were recorded as means ± standard deviation. The statistical significance between groups was determined by the unpaired two-tailed Student's t-test ($^*P < 0.05$, $^{**}P < 0.01$, $^{***}P < 0.001$).

Results and discussion

Preparation and characterization of GSH-depleting SS-Py@Ce6

The GSH-depleting polymer PEG–p(PyDSMA) and GSH-nondepleting polymer PEG–p(PyEMA) were synthesized by reversible addition–fragmentation chain transfer polymerization (RAFT), with PyDSMA (containing pyridyl disulfide groups) and PyEMA (containing pyridine groups) as monomers, respectively (Fig. S1†). The synthesis procedures of 2-methyl-2-[(dodecylsulfanylthiocarbonyl) sulfanyl] propanoic acid

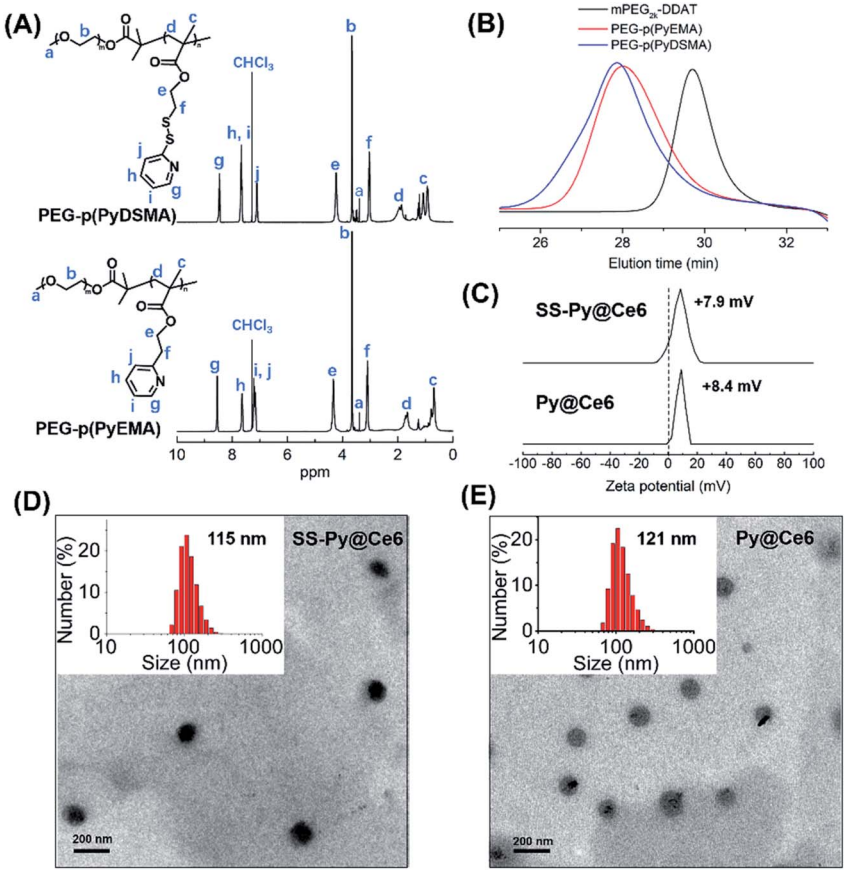

Fig. 1 Characterization of the GSH-depleting polymer and nanoparticles. (A) ^{1}H-NMR spectra of GSH-depleting polymer PEG–p(PyDSMA) and GSH-nondepleting polymer PEG–p(PyEMA) in $CDCl_3$. (B) GPC curves of macromolecular chain transfer agent mPEG$_{2k}$–DDAT, polymer PEG–p(PyEMA) and PEG–p(PyDSMA) in DMF containing LiBr (1 g L^{-1}) at a flow rate of 1.0 mL min^{-1}. (C) Zeta potentials of nanoparticles SS-Py@Ce6 and Py@Ce6. (D and E) Hydrodynamic sizes and transmission electronic microscopy (TEM) images of nanoparticles SS-Py@Ce6 and Py@Ce6. Scale bars, 200 nm.

(DDAT), macromolecular chain transfer agent $mPEG_{2k}$–DDAT, GSH-reactive monomer PyDSMA, GSH-nonreactive monomer PyEMA and the details of the RAFT reaction are described in the ESI.† The successful synthesis of chain transfer agent, monomers and polymers was verified by ^{1}H-NMR spectra (Fig. 1A and S2–S4†). The characteristic peaks of pyridine in the side chains were observed in the ^{1}H-NMR spectra of both PEG–p(PyDSMA) and PEG–p(PyEMA) polymers: 8.46–8.54 ppm, aromatic proton *ortho*-N (g), 7.63–7.68 ppm, aromatic proton *para*-N (h), 7.10–7.18 ppm, aromatic proton *ortho*-disulfide linkage (j). GPC analysis showed that PEG–p(PyDSMA) and PEG–p(PyEMA) had higher molecular weights than the macromolecular chain transfer agent $mPEG_{2k}$–DDAT (Fig. 1B). The M_n of PEG–p(PyDSMA) and PEG–p(PyEMA) were 8.6 kDa and 7.9 kDa, respectively (Fig. S5†). Both molecular weights of GSH-depleting polymer PEG–p(PyDSMA) and GSH-nondepleting polymer PEG–p(PyEMA) were uniformly distributed, with polydispersity indexes (PDI) of 1.28 and 1.22, respectively. These results suggested that PEG–p(PyDSMA) and PEG–p(PyEMA) had similar structures and molecular weights.

To investigate the loading capacity of PEG–p(PyDSMA) and PEG–p(PyEMA) polymer, photosensitizers Ce6 were encapsulated to form nanoparticles SS-Py@Ce6 and Py@Ce6, which have a similar loading contents of Ce6 of about 8.7%. Fig. 1C–E show the particle sizes, zeta potentials and morphologies of SS-Py@Ce6 and Py@Ce6. As measured by DLS, GSH-depleting SS-Py@Ce6 and GSH-nondepleting Py@Ce6 showed hydrodynamic diameters of about 115 nm and 121 nm, respectively. And they both showed positive surface charges with zeta potentials of about +7.9 mV and +8.4 mV, respectively. From the transmission electron microscopy images, SS-Py@Ce6 and Py@Ce6 nanoparticles displayed a uniformly spherical shape. In this

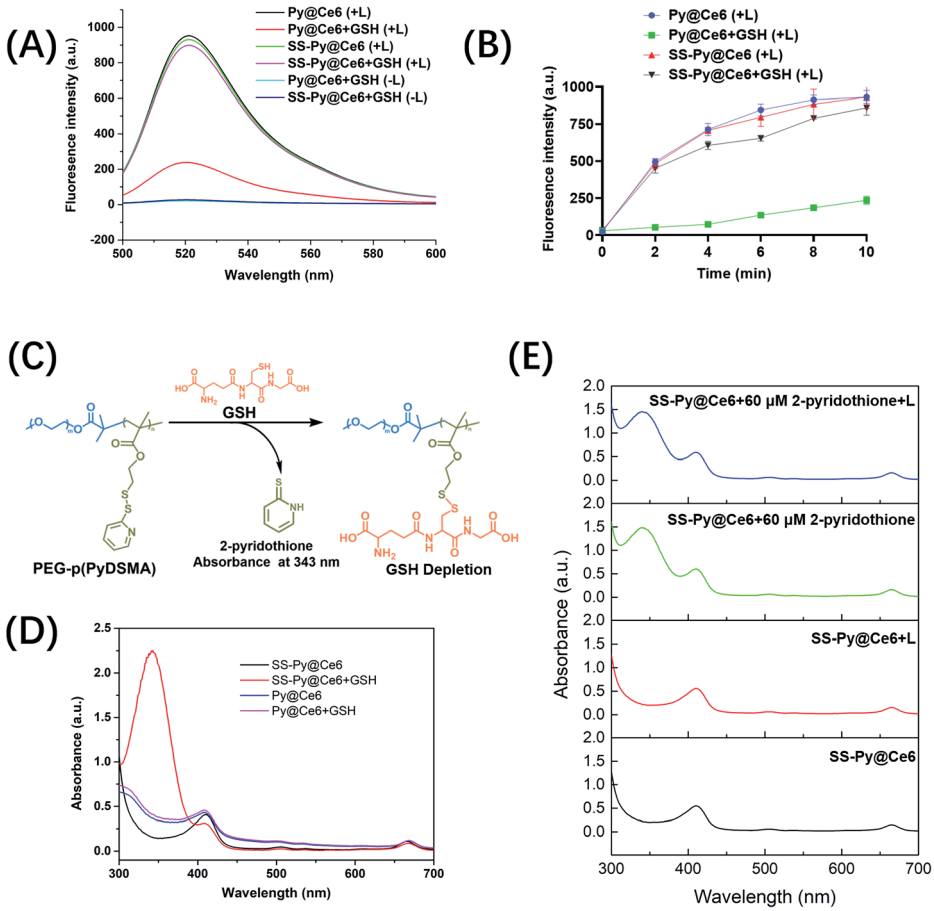

Fig. 2 Extracellular GSH depletion and ROS generation. (A) Fluorescence spectra of DCF incubated with Py@Ce6, Py@Ce6+GSH, SS-Py@Ce6, and SS-Py@Ce6+GSH with NIR irradiation (670 nm, 100 mW cm^{-2}, 10 min) and Py@Ce6+GSH, SS-Py@Ce6+GSH without NIR irradiation. The addition of 10 mM GSH was to simulate the intracellular environment of the tumor cells. The ROS generation levels were characterized by the fluorescence intensities of the fluorescent probe DCF. (B) The extracellular ROS generation of GSH-nondepleting Py@Ce6 and GSH-depleting SS-Py@Ce6 nanoparticles with and without 10 mM GSH under NIR irradiation (670 nm, 100 mW cm^{-2}) for different times (0, 2, 4, 6, 8, 10 min) (mean ± SD, $n = 3$). (C) The GSH-depleting process by the thiol–disulfide exchange reaction between PEG–p(PyDSMA) polymer and GSH. An intracellular high concentration of GSH would rapidly exchange with the pyridyl disulfide groups on the side chains of the PEG–p(PyDSMA) polymer, generating by-product 2-pyridinethione whose characteristic absorption peak in UV-vis spectra is at 343 nm. (D) UV-vis absorption spectra of Py@Ce6 and SS-Py@Ce6 with and without 10 mM GSH. GSH-nondepleting Py@Ce6 was set as a negative control. (E) UV-vis absorption spectra of SS-Py@Ce6 and SS-Py@Ce6 mixed with 60 μM 2-pyridothione with and without irradiation.

context, the Ce6-encapsulated micelles SS-Py@Ce6 and Py@Ce6 may have similar capacity in terms of Ce6-induced ROS generation due to their similar properties in particle size and morphology.

The synergistic effect on ROS level of PDT and GSH depletion

Glutathione (GSH), as a predominant antioxidant, maintains intracellular redox homeostasis by consuming oxidizing substances such as reactive oxygen species (ROS). Tumor cells are usually not susceptible to oxidative stress due to the high concentration of GSH (~10 mM), which limits the efficiency of ROS-based PDT. According to our design, SS-Py@Ce6 would synergistically increase the ROS level through NIR/Ce6-induced ROS generation and p(PyDSMA)-based GSH depletion. To verify this, the extracellular ROS levels of GSH-depleting SS-Py@Ce6 and GSH-nondepleting Py@Ce6 were detected through fluorescence spectra, with dichlorofluorescein (DCF) as the fluorescent probe. As shown in Fig. 2A, the fluorescence intensity was associated with the ROS level. Both SS-Py@Ce6 and Py@Ce6 produced a great amount of ROS under 670 nm light irradiation (100 mW cm^{-2}, 10 min) in the absence of GSH, indicating their significant photodynamic therapy effect. In the presence of 10 mM GSH, simulating the intracellular environment of tumor cells, the ROS produced by Py@Ce6 were significantly consumed by GSH, whereas the ROS produced by SS-Py@Ce6 were hardly consumed due to its GSH-depleting property, verifying that the GSH depletion induced by the PEG–p(PyDSMA) polymer may synergistically increase the intracellular ROS level. To quantitively explore the influence of GSH depletion on ROS level, the levels of ROS produced by SS-Py@Ce6 and Py@Ce6 with/without GSH were recorded at different irradiation times (0 min, 2 min, 4 min, 6 min, 8 min, 10 min) (Fig. 2B). After 2 min of irradiation, a great amount of ROS in the groups of SS-Py@Ce6, Py@Ce6 and SS-Py@Ce6+10 mM GSH were recorded, but only a small amount of ROS was detected in the Py@Ce6+10 mM GSH group. Even after 10 min of irradiation, the ROS level in the Py@Ce6+10 mM GSH group was much lower than in the other groups. This was due to the Py@Ce6-generated ROS being immediately consumed by GSH. These results demonstrated that SS-Py@Ce6 could rapidly deplete antioxidant GSH, avoiding the ROS scavenging effect by GSH.

Then we verified whether the GSH depletion was attributable to the thiol–disulfide exchange reaction between the thiol groups in GSH and the pyridyl disulfide groups in the PEG–p(PyDSMA) polymer. The exchange reaction between PEG–p(PyDSMA) polymer and GSH generated the by-product tautomeric 2-pyridinethione whose characteristic absorption peak in the UV-vis spectra was at 343 nm (Fig. 2C). From the UV-vis spectra in Fig. 2D, Py@Ce6 did not show the characteristic absorption peaks of 2-pyridinethione with/without GSH, indicating that Py@Ce6 could not react with intracellular GSH. The characteristic absorption peak at 343 nm was observed in the UV-vis spectra of SS-Py@Ce6 with GSH, whereas no obvious peak at 343 nm was recorded without GSH, confirming that the pyridyl disulfide groups on the side chains of PEG–p(PyDSMA) polymer could efficiently react with GSH and induce rapid GSH depletion. What is more, the peak of 2-pyridinethione was still not detected when SS-Py@Ce6 micelles were exposed to irradiation (670 nm, 100 mW cm^{-2}, 30 min) in the absence of GSH, suggesting that the pyridyl disulfide groups in the SS-Py@Ce6 micelles were very stable even under a high power level of NIR irradiation (Fig. 2E). The stability of by-product 2-pyridinethione was further studied. When SS-Py@Ce6 nanoparticles were mixed with 60 μM of free 2-pyridothione solution, there was almost no change in UV-vis spectra with or without irradiation, verifying that the by-product 2-pyridothione hardly reacts with ROS. These results strongly proved SS-Py@Ce6 could rapidly consume the antioxidant GSH, improving the ROS accumulation and enhancing PDT efficiency.

Efficient cellular uptake of SS-Py@Ce6

The cellular uptake efficiencies of GSH-depleting SS-Py@Ce6 and GSH-nondepleting Py@Ce6 were investigated by laser scanning confocal microscope analysis. The intracellular fluorescence of Ce6 (red) in CNE-2 cells receiving SS-Py@Ce6 and Py@Ce6 nanoparticles both gradually increased and reached a maximum 2 hours after transfection (Fig. 3A), indicating that the two nanoparticles had similar cellular internalization. CLSM images also showed that the red Ce6-fluorescence signal of SS-Py@Ce6 and Py@Ce6 nanoparticles was evenly dispersed around the nuclei stained by Hoechst 33342 (blue), suggesting that most nanoparticles were distributed in the cytoplasm. To quantitively study the cellular uptake efficiency, the CNE-2 cells receiving SS-Py@Ce6 and Py@Ce6 were subjected to flow cytometry analysis. Compared with the control group (0.06%), the majority of CNE-2 cells were successfully transfected with SS-Py@Ce6 or Py@Ce6 nanoparticles, with similar high cellular

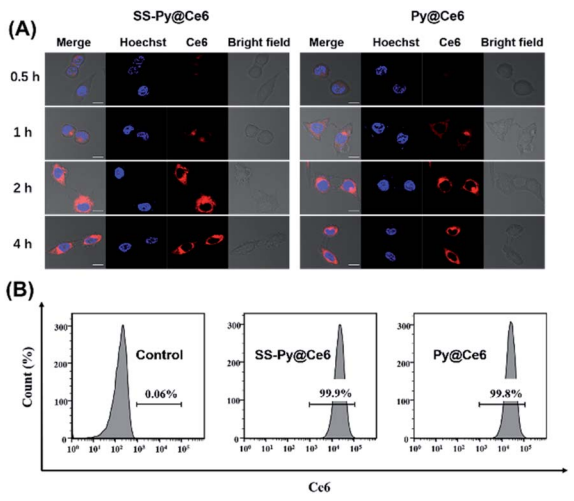

Fig. 3 Cellular uptake of nanoparticles. (A) Laser confocal microscopic images (CLSM) of CNE-2 cells treated with GSH-depleting SS-Py@Ce6 and GSH-nondepleting Py@Ce6 nanoparticles for 4 h. The cell nuclei were stained with Hoechst 33342 (blue). Nanoparticles were traced by the intrinsic red fluorescence of encapsulated Ce6. 405 nm and 640 nm were set as the excitation wavelengths of Hoechst 33342 and Ce6. Scale bar, 10 μm. (B) Flow cytometry analysis on the cellular internalization efficiency of SS-Py@Ce6 and Py@Ce6 nanoparticles.

uptake efficiencies (99.9% and 99.8% *vs.* 0.06%) (Fig. 3B), respectively.

Enhanced cytotoxicity of SS-Py@Ce6

In the process of investigating the enhanced cytotoxicity of SS-Py@Ce6, we first excluded the cytotoxicity of by-product 2-pyridothione. As shown in Fig. 4A, the viability of cells treated with free 2-pyridothione was >90% even at a high concentration (100 μg mL^{-1}), indicating that the by-product of GSH depletion causes little cytotoxicity to CEN-2 cells. We next investigated whether GSH-depleting micelles SS-Py@Ce6 could enhance the therapeutic effect of PDT (Fig. 4B). In the absence of irradiation, the treatment with GSH-nondepleting Py@Ce6 caused little cytotoxicity, whereas SS-Py@Ce6 caused a certain degree of cytotoxicity, which is probably due to the pyridyl disulfide group-induced GSH depletion. Upon NIR irradiation, the treatment with GSH-depleting SS-Py@Ce6 showed higher cytotoxicity than GSH-nondepleting Py@Ce6, indicating that the GSH-depleting SS-Py@Ce6 could synergistically enhance the PDT outcome. The above results were further confirmed by annexin V-FITC/PI flow cytometry analysis (Fig. 4C). The treatment with SS-Py@Ce6 in the absence of NIR irradiation only consumed GSH to increase the endogenous ROS, inducing a few apoptotic cells (~22.36%). The treatment with Py@Ce6 plus NIR irradiation exhibited 51.6% of apoptotic cells, which was attributed to the ROS produced by PDT. In contrast, the treatment with SS-Py@Ce6 plus NIR irradiation exhibited the biggest apoptosis rate (~95.39%), indicating GSH-depleting SS-Py@Ce6 could significantly enhance the therapeutic effect of PDT *in vitro*.

Tumor accumulation of SS-Py@Ce6

The *in vivo* distribution of SS-Py@Ce6 was studied by using the Carestream IS 4000 imaging system (Fig. 4D). To monitor the distribution of nanoparticles, the NIR fluorescent dye DiR was used in the place of Ce6 to prepare SS-Py@DiR nanoparticles. The CNE-2 tumor xenograft-bearing nude mice were intravenously injected with SS-Py@DiR nanoparticles at a DiR dose of 400 μg kg^{-1}. Then the fluorescence distribution of the nanoparticles was recorded at certain different time points (0, 3, 6, 9, 12, 24 and 48 h post injection). The fluorescence signals reached a maximum at the tumor tissue 6 h after injection. From observation of fluorescence in the excised organs (Fig. S6†), SS-Py@DiR nanoparticles were mainly distributed in tumor tissues, with some nanoparticles in the liver, and almost no nanoparticles in the heart, spleen, lung, or kidneys. These results proved that the GSH-depleting SS-Py@Ce6 nanoparticles could effectively accumulate in tumor tissue.

Improvement of ROS levels induced by GSH depletion *in vitro*

The lethality of PDT to tumor cells depends on the ROS levels generated by photosensitizers under irradiation. The

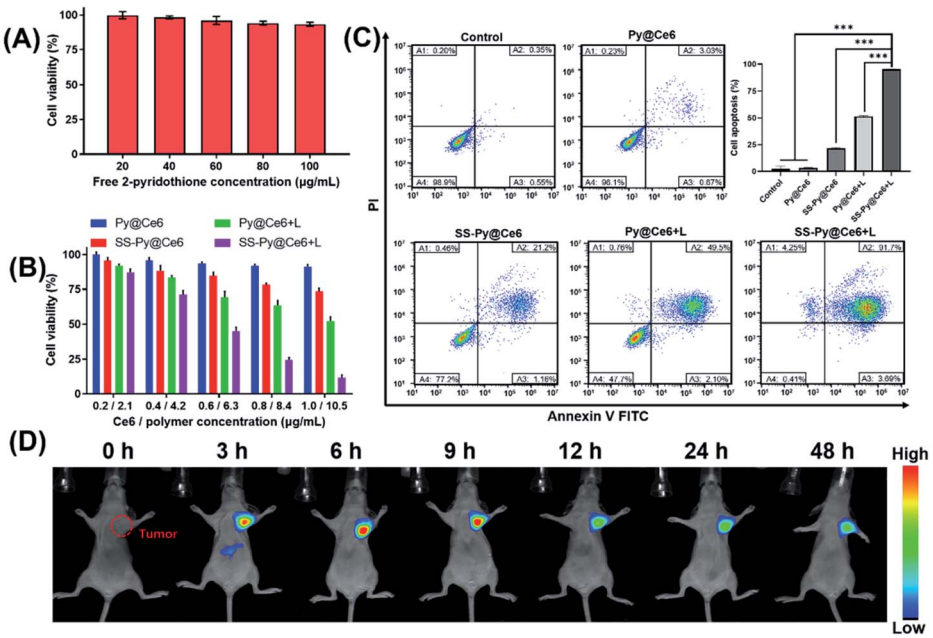

Fig. 4 Enhancing PDT *via* GSH-depleting nanoparticles *in vitro* and the biodistribution of nanoparticles *in vivo*. (A) Cytotoxicity of free 2-pyridinethione to CNE-2 cells at different concentrations (20, 40, 60, 80 and 100 μg mL^{-1}) (mean ± SD, $n = 3$). (B) Cytotoxicity of SS-Py@Ce6 and Py@Ce6 to CNE-2 cells at different Ce6/polymer concentrations (0.2/2.1, 0.4/4.2, 0.6/6.3, 0.8/8.4, and 1.0/10.5 μg mL^{-1}) with and without NIR irradiation (670 nm, 100 mW cm^{-2}, 2 min) (mean ± SD, $n = 3$). (C) Apoptosis analysis of CNE-2 cells treated with SS-Py@Ce6 and Py@Ce6 with and without NIR irradiation (670 nm, 100 mW cm^{-2}, 2 min). (A1: dead cells, A2: late apoptotic cells, A3: normal cells, A4: early apoptotic cells). The cell apoptosis rates of the A2 and A3 quadrants were recorded statistically. Untreated cells were set as the control group (mean ± SD, $n = 3$). ***$P < 0.001$. (D) *In vivo* biodistribution of GSH-depleting nanoparticles SS-Py@Ce6. NIR fluorescent dye encapsulated SS-Py@DiR was intravenously injected into the tumor-bearing mice at the DiR dose of 400 μg kg^{-1}. The fluorescence images were recorded at different time points (0, 3, 6, 9, 12, 24 and 48 h) after injection. The red circle indicates the location of the tumor.

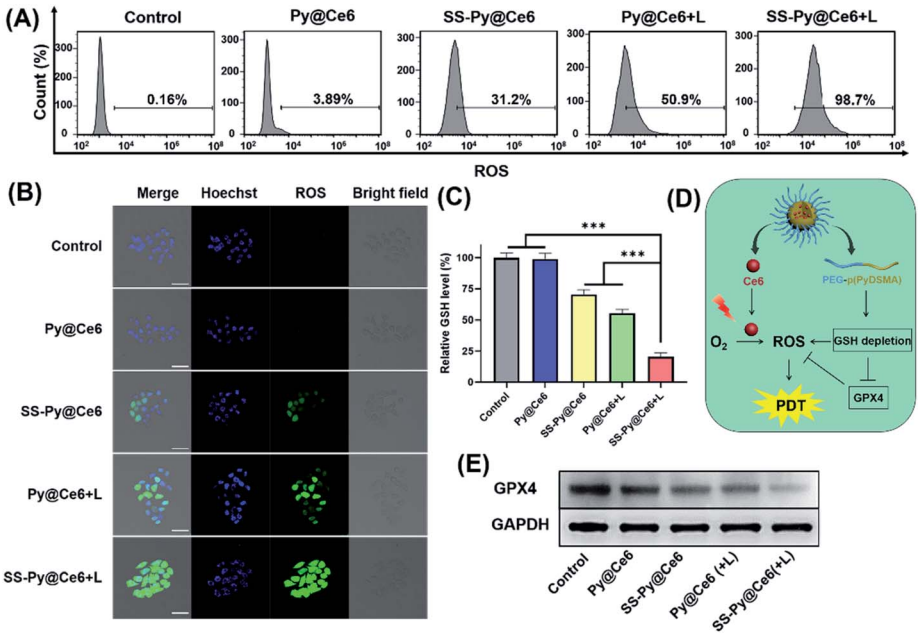

Fig. 5 Enhanced ROS generation by GSH-depleting nanoparticles loaded with Ce6 *in vitro*. (A) Flow cytometry analysis of intracellular ROS levels in the cells receiving various treatments (PBS, Py@Ce6, SS-Py@Ce6, Py@Ce6+L, SS-Py@Ce6+L). (B) CLSM images of ROS generation in CNE-2 cells incubated with SS-Py@Ce6 and Py@Ce6 with and without NIR irradiation (670 nm, 100 mW cm^{-2}, 2 min). Untreated cells were used as the control group. Scale bar, 50 μm. (C) The relative GSH levels in cells receiving different treatments (PBS, Py@Ce6, SS-Py@Ce6, Py@Ce6+L, SS-Py@Ce6+L) (mean ± SD, $n = 3$). ***$P < 0.001$. (D) Mechanism of enhancing PDT through GSH-depleting nanoparticle SS-Py@Ce6. The disulfide–thiol exchange between the pendant pyridyl disulfide groups in PEG–p(PyDSMA) and the thiols groups in GSH efficiently consumed GSH. GSH depletion downregulated glutathione peroxidase 4 (GPX4) expression, improving ROS accumulation and enhancing the PDT effect. (E) Western blotting analysis of GPX4 protein in CNE-2 cells treated with PBS, Py@Ce6, SS-Py@Ce6, Py@Ce6+L and SS-Py@Ce6+L.

intracellular ROS generation level of SS-Py@Ce6 nanoparticles was detected by confocal laser scanning microscopy (CLSM) and flow cytometry analysis, with DCFH-DA as the ROS probe (Fig. 5A and B). There was no obvious fluorescence signal in the cells receiving Py@Ce6 without light irradiation (3.89%), which was similar to the control group (0.16%). A certain amount of ROS fluorescence (31.2%) was exhibited in the CNE-2 cells receiving SS-Py@Ce6 without irradiation due to the increased endogenous ROS by GSH depletion. Under 670 nm light irradiation, the cells receiving Py@Ce6 and SS-Py@Ce6 showed obvious fluorescence signals. According to the flow cytometry analysis, the intracellular ROS level of the cells receiving SS-Py@Ce6 with irradiation was much higher (98.7%) than that of Py@Ce6 (50.9%), indicating that SS-Py@Ce6 could enhance the intracellular ROS level.

To further investigate whether the enhanced intracellular ROS level is attributable to GSH depletion, the GSH levels of CNE-2 cells receiving different treatments were measured. As shown in Fig. 5C, the GSH-depleting micelles SS-Py@Ce6 without irradiation can decrease the GSH levels of CNE-2. Under NIR irradiation, both SS-Py@Ce6 and Py@Ce6 can decrease the GSH levels of CNE-2 by Ce6-generated ROS. However, the SS-Py@Ce6 showed the lowest level of GSH, which was due to the combination of the pyridyl disulfide group-induced GSH depletion and PDT. It was reported[35,47,48] that GSH depletion can improve ROS accumulation through inhibiting glutathione peroxidase 4 (GPX4) expression (Fig. 5D). Thus, western blot analysis of GPX4 in CNE-2 receiving different treatments was used to further confirm the GSH depletion (Fig. 5E), which was consistent with the GSH levels of the CNE-2 cells receiving different treatments. These results proved that SS-Py@Ce6 could effectively deplete GSH and increase the intracellular ROS level, thus improving the PDT effect.

Anti-tumor efficiency of SS-Py@Ce6 *in vivo*

Encouraged by the *in vitro* results of GSH-depleting nanocarrier and Ce6-based PDT, we studied the *in vivo* antitumor efficacy of SS-Py@Ce6 nanoparticles. The CNE-2 tumor xenograft-bearing nude mice were randomly divided into five groups ($n = 5$): PBS (negative control), GSH-nondepleting Py@Ce6 without NIR irradiation (Py@Ce6), GSH-nondepleting Py@Ce6 with NIR irradiation (Py@Ce6+L), GSH-depleting SS-Py@Ce6 without NIR irradiation (SS-Py@Ce6), and GSH-depleting SS-Py@Ce6 with NIR irradiation (SS-Py@Ce6+L). The *in vivo* tumor accumulation results of SS-Py@DiR nanoparticles showed that the highest signal intensity of dye DiR in the tumor tissue appeared 6 hours post injection (Fig. 4D), so the NIR irradiation at a wavelength of 670 nm was performed 6 h after nanoparticle injection. The Py@Ce6 treatment without NIR irradiation hardly inhibited the tumor growth. In contrast, the SS-Py@Ce6, Py@Ce6+L and SS-Py@Ce6+L treatments reduced the tumor volumes by 38.1, 65.1, and 88.2%, and reduced the tumor weights by 43.6, 67.5, and 91.0%, compared with the Py@Ce6 treatment 18 days after the first nanoparticle injection (Fig. 6A–C). The SS-Py@Ce6+L

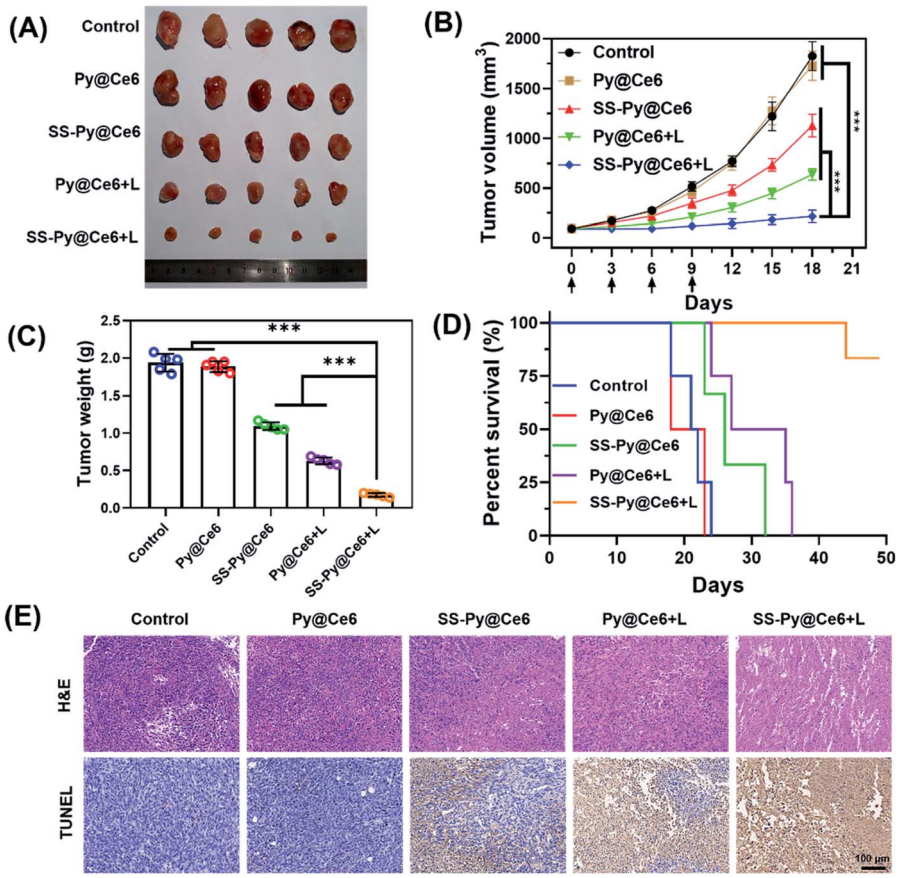

Fig. 6 Anti-tumor efficiency of GSH-depleting nanoparticles loaded with Ce6 *in vivo*. (A) Digital image of excised tumor tissues from mice receiving different treatments. CNE-2 xenograft tumor-bearing nude mice were divided into 5 groups and intravenously injected with Py@Ce6 or SS-Py@Ce6 nanoparticles at a Ce6 dosage of 2 mg kg^{-1}. NIR irradiation was performed at the tumor site (670 nm, 0.1 W cm^{-2}, 10 min). The mice were sacrificed 18 days after first drug injection (mean ± SD, $n = 5$). (B) Tumor growths in CNE-2 xenograft tumor-bearing nude mice. The diameters of the tumors were measured with vernier callipers every 3 days after first drug injection (mean ± SD, $n = 5$). ***$P < 0.001$. Black arrows indicate intravenous injection times. (C) Tumor weights in CNE-2 xenograft tumor-bearing mice receiving different treatments (mean ± SD, $n = 5$). ***$P < 0.001$. (D) Survival rate of CNE-2 xenograft tumor-bearing nude mice receiving different treatments. Mice were euthanized when tumor volumes reached 2000 mm^3. (E) H&E- and TUNEL-stained tumor tissue sections from mice receiving different treatments. H&E staining: cell nuclei were stained blue; the extracellular matrix and cytoplasm were stained red. TUNEL staining: normal tumor cells were stained green; apoptotic cells were stained brown. Scale bar, 100 μm.

treatment showed greater antitumor inhibition effect than any other treatment, which was due to the combinatory effect of NIR/Ce6-induced ROS generation and the pyridyl disulfide group-induced GSH depletion. All the mice receiving Py@Ce6 survived less than 25 days, similar to the control group. Over half of the mice in the groups of SS-Py@Ce6 and Py@Ce6+L died within 30 d, and the rest of them did not survive longer than 36 days (Fig. 6D). Notably, over 80% of the mice receiving SS-Py@Ce6+L survived longer than 50 d, suggesting the significant anti-tumor effect of PDT enhanced by GSH depletion. Histological H&E staining and apoptotic TUNEL assays (Fig. 6E) revealed that the treatment of SS-Py@Ce6 under irradiation induced the highest degree of cell necrosis and apoptosis. The major organs of mice receiving different treatment did not exhibit pathological changes (Fig. S7†). These *in vivo* results proved that SS-Py@Ce6 nanoparticles can induce GSH consumption, making a tumor more susceptible to oxidative stress, which significantly enhances the effect of PDT.

Conclusions

In this work, we designed a novel GSH-depleting nanocarrier to efficiently deliver the hydrophobic photosensitizer Ce6 and significantly enhance the therapeutic efficacy of PDT. The nanocarriers showed satisfactory Ce6 loading content and a great capacity to generate ROS. The pendant pyridyl disulfide groups on the side chain of the GSH-depleting copolymer effectively consumed the high concentration of GSH in tumor cells. The GSH depletion broke the redox homeostasis and promoted the intracellular ROS level, exhibiting significantly enhanced cytotoxicity and apoptosis. This study details an efficient and straightforward strategy for enhancing the PDT effect.

Author contributions

Shi-yin Wang and Guo Chen contributed equally to this work. Shi-yin Wang: investigation, validation, writing – review &

editing. Guo Chen: methodology, validation. Ji-feng Chen: validation. Jin Wang: funding acquisition. Shao-hui Deng*: methodology, supervision. Du Cheng*: conceptualization, supervision.

Conflicts of interest

There are no conflicts to declare.

Acknowledgements

This work was financially supported by the National Natural Science Foundation of China (21875289 and 91959118) and the National Natural Science Foundation of Guangdong Province (2022A1515011304).

Notes and references

1 J. M. Chen, T. J. Fan, Z. J. Xie, Q. Q. Zeng, P. Xue, T. T. Zheng, Y. Chen, X. L. Luo and H. Zhang, *Biomaterials*, 2020, **237**, 119827.
2 A. Master, M. Livingston and A. Sen Gupta, *J. Controlled Release*, 2013, **168**, 88–102.
3 S. Kwiatkowski, B. Knap, D. Przystupski, J. Saczko, E. Kedzierska, K. Knap-Czop, J. Kotlinska, O. Michel, K. Kotowski and J. Kulbacka, *Biomed. Pharmacother.*, 2018, **106**, 1098–1107.
4 E. Ostasnka, D. Aebisher and D. Bartusik-Aebisher, *Biomed. Pharmacother.*, 2021, **137**, 111302.
5 Z. J. Zhou, J. B. Song, L. M. Nie and X. Y. Chen, *Chem. Soc. Rev.*, 2016, **45**, 6597–6626.
6 W. Zhang, J. Lu, X. N. Gao, P. Li, W. Zhang, Y. Ma, H. Wang and B. Tang, *Angew. Chem., Int. Ed.*, 2018, **57**, 4891–4896.
7 I. Yakavets, M. Millard, V. Zorin, H. P. Lassalle and L. Bezdetnaya, *J. Controlled Release*, 2019, **304**, 268–287.
8 M. G. Mokwena, C. A. Kruger, M. T. Ivan and A. Heidi, *Photodiagn. Photodyn. Ther.*, 2018, **22**, 147–154.
9 S. H. Deng, X. X. Li, S. Liu, J. F. Chen, M. Q. Li, S. Y. A. Chew, K. Leong and D. Cheng, *Sci. Adv.*, 2020, **6**, eabb4005.
10 C. Hu, X. Q. He, Y. X. Chen, X. T. Yang, L. Qin, T. Lei, Y. Zhou, T. Gong, Y. Huang and H. L. Gao, *Adv. Funct. Mater.*, 2021, 31.
11 M. Shu, J. J. Tang, L. L. Chen, Q. Zeng, C. Li, S. T. Xiao, Z. Z. Jiang and J. Liu, *Biomaterials*, 2021, 268.
12 M. A. Rajora, J. W. H. Lou and G. Zheng, *Chem. Soc. Rev.*, 2017, **46**, 6433–6469.
13 H. B. Cheng, B. Qiao, H. Li, J. Cao, Y. L. Luo, K. M. K. Swamy, J. Zhao, Z. G. Wang, J. Y. Lee, X. J. Liang and J. Yoon, *J. Am. Chem. Soc.*, 2021, **143**, 2413–2422.
14 J. Z. Zhao, K. J. Xu, W. B. Yang, Z. J. Wang and F. F. Zhong, *Chem. Soc. Rev.*, 2015, **44**, 8904–8939.
15 J. Zhou, Y. Z. Zhang, G. C. Yu, M. R. Crawley, C. R. P. Fulong, A. E. Friedman, S. Sengupta, J. F. Sun, Q. Li, F. H. Huang and T. R. Cook, *J. Am. Chem. Soc.*, 2018, **140**, 7730–7736.
16 S. S. Lucky, K. C. Soo and Y. Zhang, *Chem. Rev.*, 2015, **115**, 1990–2042.
17 F. Hu, S. D. Xu and B. Liu, *Adv. Mater.*, 2018, **30**, 1801350.
18 C. F. van Nostrum, *Adv. Drug Delivery Rev.*, 2004, **56**, 9–16.
19 F. Y. Zhou, B. Feng, H. J. Yu, D. G. Wang, T. T. Wang, Y. T. Ma, S. L. Wang and Y. P. Li, *Adv. Mater.*, 2019, 31.
20 S. Moghassemi, A. Dadashzadeh, R. B. Azevedo, O. Feron and C. A. Amorim, *J. Controlled Release*, 2021, **339**, 75–90.
21 P. T. Schumacker, *Cancer Cell*, 2015, **27**, 156–157.
22 Y. J. Huang, Y. L. Jiang, Z. H. Xiao, Y. F. Shen, L. F. Huang, X. Y. Xu, G. F. Wei, C. J. Xu and C. S. Zhao, *Chem. Eng. J.*, 2020, 380.
23 M. M. Chen, D. P. Liu, F. S. Liu, Y. N. Wu, X. J. Peng and F. L. Song, *J. Controlled Release*, 2021, **332**, 269–284.
24 Y. X. Xiong, C. Xiao, Z. F. Li and X. L. Yang, *Chem. Soc. Rev.*, 2021, **50**, 6013–6041.
25 T. Su, F. R. Cheng, Y. J. Pu, J. Cao, S. B. Lin, G. Z. Zhu and B. He, *Chem. Eng. J.*, 2021, **411**, 128561.
26 J. Feng, J. L. Gao, R. Y. Zhang, W. X. Ren and Y. B. Dong, *ACS Appl. Bio Mater.*, 2020, **3**, 8667–8675.
27 J. H. Shi, T. R. Wang, Y. Q. You, M. L. Akhtar, Z. J. Liu, F. Han, Y. Li and Y. Wang, *Nanoscale*, 2019, **11**, 13078–13088.
28 F. R. Liu, S. L. Gong, M. L. Shen, T. He, X. Q. Liang, Y. Q. Shu, X. X. Wang, S. Ma, X. C. Li, M. M. Zhang, Q. J. Wu and C. Y. Gong, *Chem. Eng. J.*, 2021, **403**, 126305.
29 J. Deng, F. Liu, L. Wang, Y. An, M. Gao, Z. Wang and Y. Zhao, *Biomater. Sci.*, 2019, **7**, 429–441.
30 K. Cherukula, K. Manickavasagam Lekshmi, S. Uthaman, K. Cho, C.-S. Cho and I.-K. Park, *Nanomaterials*, 2016, **6**, 76.
31 C. M. Saporito-Magrina, R. N. Musacco-Sebio, G. Andrieux, L. Kook, M. T. Orrego, M. V. Tuttolomondo, M. F. Desimone, M. Boerries, C. Borner and M. G. Repetto, *Metallomics*, 2018, **10**, 1743–1754.
32 H. Cao, S. Zhong, Q. Wang, C. Chen, J. Tian and W. Zhang, *J. Mater. Chem. B*, 2020, **8**, 478–483.
33 M. Monfared, M. D. Nothling, D. Mawad and M. H. Stenzel, *Biomacromolecules*, 2021, **22**, 4295–4305.
34 X. Xiao, K. W. Wang, Q. Y. Zong, Y. L. Tu, Y. S. Dong and Y. Y. Yuan, *Biomaterials*, 2021, 270.
35 X. Meng, J. Deng, F. Liu, T. Guo, M. Y. Liu, P. P. Dai, A. P. Fan, Z. Wang and Y. J. Zhao, *Nano Lett.*, 2019, **19**, 7866–7876.
36 L. B. Ke, F. M. Wei, X. X. Liao, T. W. Rees, S. Kuang, Z. Liu, Y. Chen, L. N. Ji and H. Chao, *Nanoscale*, 2021, **13**, 7590–7599.
37 Z. H. Zhang, Y. X. Ding, Y. J. Li, P. Wu, J. Guo and C. C. Wang, *Adv. Ther.*, 2019, **2**, 1800113.
38 K. Li, W. Y. Dong, Y. X. Miao, Q. Z. Liu, L. Qiu and J. G. Lin, *J. Photochem. Photobiol., B*, 2021, 215.
39 I. Altinbasak, M. Arslan, R. Sanyal and A. Sanyal, *Polym. Chem.*, 2020, **11**, 7603–7624.
40 R. Bej, A. Ghosh, J. Sarkar, B. B. Das and S. Ghosh, *ChemBioChem*, 2020, **21**, 2921–2926.
41 Y. L. Yang, Y. Li, Q. N. Lin, C. Y. Bao and L. Y. Zhu, *ACS Macro Lett.*, 2016, **5**, 301–305.
42 M. Geven, H. Luo, D. Koo, G. Panambur, R. Donno, A. Gennari, R. Marotta, B. Grimaldi and N. Tirelli, *ACS Appl. Mater. Interfaces*, 2019, **11**, 26607–26618.
43 X. T. Cheng, H. D. Xu, H. H. Ran, G. L. Liang and F. G. Wu, *ACS Nano*, 2021, **15**, 8039–8068.

44 B. Y. Niu, K. X. Liao, Y. X. Zhou, T. Wen, G. L. Quan, X. Pan and C. B. Wu, *Biomaterials*, 2021, 277.
45 P. Zhang, J. Li, M. Ghazwani, W. C. Zhao, Y. X. Huang, X. L. Zhang, R. Venkataramanan and S. Li, *Biomaterials*, 2015, **67**, 104–114.
46 Q. Zhang, X. L. Wang, P. Z. Li, K. T. Nguyen, X. J. Wang, Z. Luo, H. C. Zhang, N. S. Tan and Y. L. Zhao, *Adv. Funct. Mater.*, 2014, **24**, 2450–2461.
47 J. Chen, F. Chen, L. Zhang, Z. Yang, T. Deng, Y. Zhao, T. Zheng, X. Gan, H. Zhong, Y. Geng, X. Fu, Y. Wang and C. Yu, *ACS Appl. Mater. Interfaces*, 2021, **13**, 27856–27867.
48 K. C. Liang, H. T. Sun, Z. B. Yang, H. Z. Yu, J. Shen, X. L. Wang and H. R. Chen, *Adv. Funct. Mater.*, 2021, 31.